We are IntechOpen,
the world's leading publisher of Open Access books
Built by scientists, for scientists

5,000
Open access books available

125,000
International authors and editors

140M
Downloads

Our authors are among the

154
Countries delivered to

TOP 1%
most cited scientists

12.2%
Contributors from top 500 universities

CLARIVATE ANALYTICS
BOOK CITATION INDEX
INDEXED

WEB OF SCIENCE™

Selection of our books indexed in the Book Citation Index
in Web of Science™ Core Collection (BKCI)

Interested in publishing with us?
Contact book.department@intechopen.com

Numbers displayed above are based on latest data collected.
For more information visit www.intechopen.com

Vertical-Type Organic Light-Emitting Transistors with High Effective Aperture Ratios

Byoungchoo Park, Won Seok Lee, Seo Yeong Na, Jaewoo Park and In-Gon Bae

Abstract

The inherent complexity of the structures of active-matrix (AM) organic light-emitting diode (OLED) displays severely limits not only their size but also device performance. Surface-emitting organic light-emitting transistors (OLETs) may offer an attractive alternative to AM displays. We report some characteristics of vertical-type OLETs (VOLETs) composed of a source electrode of low-dimensional materials and an emissive channel layer. With a functionalized graphene source, it is shown that the full-surface electroluminescent emission of a VOLET can be effectively controlled by the gate voltage with a high luminance on/off ratio (10^4). The current efficiency and effective aperture ratios were observed to be more than 150% of those of a control OLED, even at high luminances exceeding 500 cd m^{-2}. Moreover, high device performance of micro-VOLET pixels has been also successfully demonstrated using inkjet-patterned emissive channel layers. These significant improvements in the device performance were attributed to the effective gate-voltage-induced modulation of the hole tunneling injection at the source electrode.

Keywords: organic light-emitting diode (OLED), organic light-emitting transistor (OLET), vertical-type OLETs, graphene, on/off ratio, aperture ratio, inkjet printing, tunneling injection

1. Introduction

In recent years, researchers of state-of-the-art electronics utilizing organic semiconducting materials have succeeded in advancing various devices, such as organic light-emitting diodes (OLEDs), photovoltaic cells, organic thin-film transistors (OTFTs), and sensors, among others [1–10]. Among these, intensive efforts in OLEDs have led to high brightness, efficiency, and full-color electroluminescent (EL) emissions for various light-emitting optoelectronic devices [7–10]. The advantages of such OLEDs over conventional liquid crystal displays (LCDs) are well known, especially for high-quality displays in terms of their viewing angle, response time, thickness, and contrast ratio [11]. For instance, small OLED displays are constructed on an array of thin-film transistor (TFT) switches, allowing precise control of the states of the pixels [12–14]. In such active-matrix OLEDs (AM-OLEDs), the OLED is driven in the current mode; thus, at least two TFTs, in this case a switching TFT to select a pixel and a driving TFT to operate the OLED, are required, as shown

in **Figure 1(a)** [12, 13]. Perhaps unexpectedly, however, the complexity of such pixel circuit designs with their sophisticated procedures has led to a significantly limited light-emitting area and aperture ratio (the light-emitting area as a fraction of the total area of the device, typical aperture ratios: 25–34%) [13–15], introducing severe problems associated with limited device performance and limited display sizes for AM-OLEDs. Besides these issues, fundamental factors related to the architecture of the OLED itself, such as exciton quenching and photon loss, also still limit the efficiency and brightness of these devices.

To overcome some of the limitations of (AM-)OLEDs, research on different structures and materials is currently yielding new developments [15–30]. Among these, organic light-emitting transistors (OLETs), such as static-induction-transistor OLETs (SIT-OLETs) [17, 18], metal-insulator-semiconductor OLETs (MIS-OLETs) [19], lateral-type OLETs [20–29], and vertical-type OLETs (VOLETs) [30], have been devised by integrating the capability of the OLED to generate EL light with the switching functionality of a field-effect transistor (FET) into a single device structure. In these OLETs, the current that flows through emissive semiconductor channel layers can be controlled by the gate voltage, which can also change the EL emission brightness state from the dark off- to the bright on-state. The on-state implies that holes and electrons injected into the channel layer form excitons that recombine radiatively to generate EL light [17–30]. These OLETs are of key interest; not only do they provide a novel device architecture to investigate fundamental optoelectronic properties related to charge carrier injection, transport, and radiative exciton recombination processes in organic semiconducting materials, at the same time OLETs can also be used to develop highly integrated organic optoelectronic devices such as highly bright and efficient light sources, optical communication systems, and electrically driven organic lasers [21–30].

In principle, the luminance from OLETs can be modulated by the gate voltage without any additional driving devices; thus, displays using OLETs have the advantage of greatly reducing both the number of TFTs and the circuit complexity (**Figure 1(b)**), thereby providing an effective means of increasing the aperture ratio [29]. Hence, OLETs could be a key part of the development of next-generation AM display technology [29]. Indeed, a proof-of-principle device was recently developed using carbon nanotubes (CNTs, **Figure 2**), delivering a CNT-based vertical-type OLET (CNT-VOLET) [31–34]. In the CNT-VOLET, a dilute network of CNTs is used as a source electrode, leading to several improvements, such as a high on/off ratio, attributed to the gate-bias-induced modulation of the lateral (or horizontal) Schottky barrier height [31, 32]. Nevertheless, the improvement of the effective aperture ratio (AR_{eff}, the percentage ratio of the current efficiency of a surface emitting OLET to that of a control ITO-base OLED at a given luminance) in the
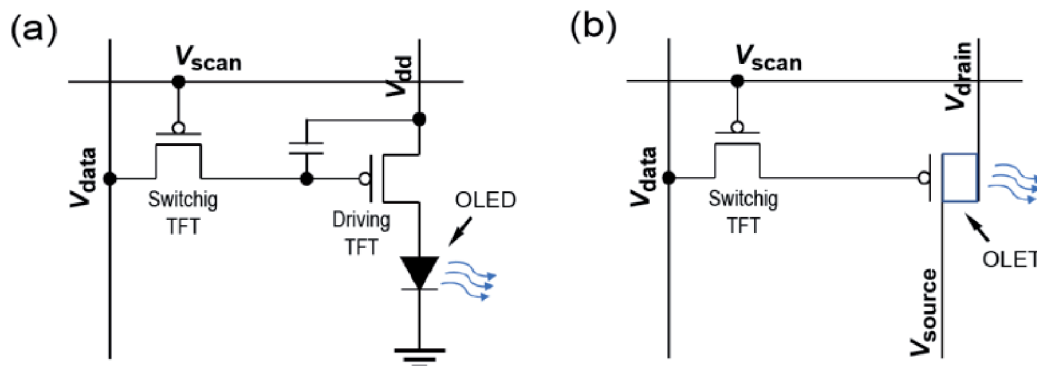

Figure 1.
(a) A conventional two TFTs + one capacitor AM-OLED pixel circuit diagram with a switching TFT and driving TFT. (b) A simple AM-OLET pixel circuit of an integrated OLET and a switching TFT.
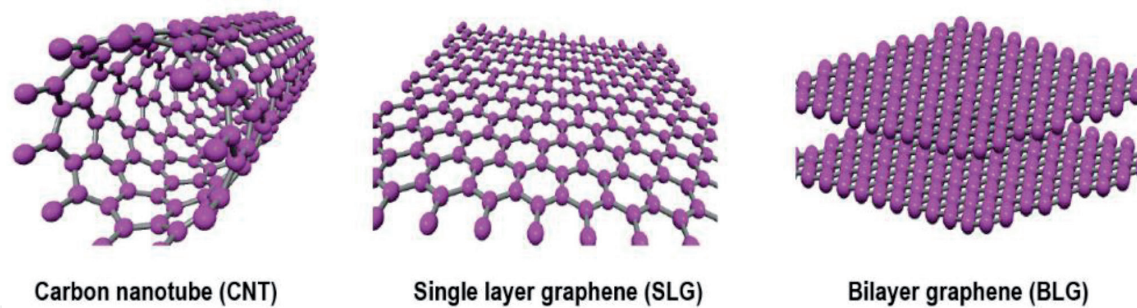
Figure 2.
The structure of carbon nanotube (CNT), single-layer graphene (SLG), and bilayer graphene (BLG).

CNT-VOLET is still limited to less than those of control OLEDs, and its parasitic power consumption (*PPC*, percentage of power dissipated across the driving transistor element of the device not contributing to light generation) requires further reductions [32]. Moreover, this attempt resulted in a complicated source structure, and the production of porous CNT network sources with smooth and homogeneous surfaces was problematic due to the aggregation of CNTs [35]; significant obstacles thus remain with regard to the limited reproducibility of these devices. Thus, the goal of high-performance and reliable OLETs with high AR_{eff} and low *PPC* values remains a considerable challenge.

In this chapter, for the VOLET, the use of a nonporous, homogeneous, smooth, and easily processable graphene layer is described as the source contact, together with an emissive channel layer. Here, the graphene is a two-dimensional (2D) material in the form of a single atomic layer of carbon with a hexagonal lattice structure bonded in the sp^2 configuration (**Figure 2**) [36–38]. Despite the similar low dimensionality of graphene to CNTs [36, 37], the optoelectric properties of a VOLET based on graphene have not yet been fully characterized. Herein, the fabrication and characterization are described for a simple VOLET with a single-layer graphene (SLG) source contact (Gr-VOLET), capable of efficiently modulating device performance levels with high luminance on/off ratios (~10^4) upon the application of a gate voltage. The Gr-VOLETs with doped SLG sources with $FeCl_3$ are demonstrated to exhibit greatly improved device performance, especially in their enhanced current efficiency and AR_{eff} values of more than 150% of those of a control OLED, even at high EL luminance levels exceeding 500 cd m^{-2}. These figures are among the highest ever published for OLETs, and their low *PPC*s make them all the more attractive. Moreover, such high device performance has also been successfully confirmed even for micro-VOLET pixels fabricated by an inkjet-patterning technique [39].

2. 2D material electrode: doped CVD graphene

2.1 Preparation of SLG source electrodes

Preparation of substrates: The transparent VOLET substrate used here was prepared with a pre-patterned bottom gate electrode, consisting of a transparent ITO layer (80-nm-thick, 30 ohm square^{-1} sheet resistance) on a glass substrate, and a sputter-deposited aluminum oxide (Al_2O_3) top layer (400 nm) as a gate dielectric over the ITO gate (glass/ITO/Al_2O_3). The VOLET substrate used was then cleaned with alcohol, followed by a UV treatment (5 min), prior to the fabrication of the devices.

Synthesis and transfer of SLG: The procedure used for transferring the chemical-vapor-deposition (CVD)-grown graphene onto a target substrate [40–45], in this case an FET substrate, a VOLET substrate, or a glass substrate, is described below. The first

step involves the CVD growth of graphene on a copper (Cu) foil [42–45]. A clean Cu foil was placed in a quartz tube vacuum chamber and then the temperature of the chamber was increased to 1000°C under Ar (10 sccm). For the growth of graphene, a mixed gas of methane (CH_4, 30 sccm) and hydrogen (H_2, 10 sccm) was used at approximately 2.7×10^{-2} Pa. The next step involved spin-coating a solution of poly-methyl methacrylate (PMMA) at 3000 rpm for 60 s onto the graphene on the Cu foil [42–45]. The graphene on the back side of the Cu foil was removed by atmospheric-pressure oxygen plasma. Next, a PMMA-coated Cu/Gr (Cu/Gr/PMMA) block (width: 4 mm, length: 20 mm) was floated on an aqueous $FeCl_3$ etching solution used to etch the Cu foil entirely, at 50°C for 20 min [40]. Next, the Gr/PMMA block was rinsed with deionized (DI) water two to five times (10 min) and transferred onto a target substrate, after which the graphene-transferred substrate was dried under reduced pressure (~1 Pa) for 1 h and left in air for 24 h. The PMMA layer was then removed by dissolving the PMMA layer in chloroform (~60 min), monochlorobenzene (~30 min), and chloroform again (~30 min), to obtain a SLG source electrode. The optical characteristics of the SLG-transferred VOLET substrate were monitored using a UV–visible spectroscopy system. The average optical transmittance (~92%) of a SLG source on a VOLET substrate in the visible range (400–800 nm) was found to be similar to that (~92%) of a conventional ITO-coated glass substrate for OLEDs.

2.2 Characterization of SLGs

In this study, a transferred SLG was investigated as a source contact, where the $FeCl_3$ doping is processed spontaneously during the graphene transfer process [40]. The basic properties of the three SLG sources are shown in **Figures 3** and **4** and are summarized in **Table 1**.

In order to identify the SLG used, the surface composition of the SLG on the SiO_2/Si substrates was analyzed by X-ray photoelectron spectroscopy (XPS). **Figure 3(a)** presents the wide-scan XPS spectra, showing strong photoelectron lines at binding energies of ~104, ~285, and ~531 eV, which are attributed to Si2p, C1s and O1s, respectively. Note that there is no Cu peak in the range of 932–935 eV (Cu2p and Cu^{2+}), implying the complete etching of the Cu foil. In addition, the XPS spectra also revealed small but measurable amounts of Cl and Fe. These are likely residues of the etchant ($FeCl_3$) used during the etching process. When such $FeCl_3$ residues adsorb onto the SLG, the transfer of electrons to the Cl from the SLG (chlorination) [46] induces unintentional p-doping of the SLG.

Figure 3(b) shows the surface morphology of the SLG on the VOLET substrate as measured by a noncontact atomic force microscope (AFM). As indicated by the AFM morphology, the SLG samples exhibit a fairly smooth surface; the SLG presented an AFM morphology that was nearly identical at different positions on the investigated SLG samples with low RMS roughness levels of 1.4–2.0 nm.

The surface-contact potential difference (V_{CPD}) of the SLG on the VOLET substrate was also monitored using a simultaneous Kelvin probe force microscope (KPFM) by applying AC voltage (1 V) with a frequency of 18 kHz to a Pt/Ir-coated silicon KPFM cantilever. In order to calibrate the work function of the sample, V_{CPD} of highly oriented pyrolytic graphite (HOPG) was used as a reference V_{CPD}. The work function of the SLG (W_{SLG}) was obtained by a comparison of V_{CPD}s for the SLG and the HOPG,

$$W_{SLG} = W_{HOPG} + [V_{CPD}(\text{HOPG}) - V_{CPD}(\text{SLG})], \qquad (1)$$

where W_{HOPG} is the work function of the HOPG (~4.6 eV) [47]. **Figure 3(c)** shows the distributions of the work functions of the SLG as measured by the KPFM. The estimated average work function of the $FeCl_3$-doped SLG on the VOLET

substrate is approximately 5.21 ± 0.07 eV, which is higher than the intrinsic work function (4.5–4.8 eV) of undoped monolayer graphenes [47, 48], mainly due to the $FeCl_3$ doping [49].
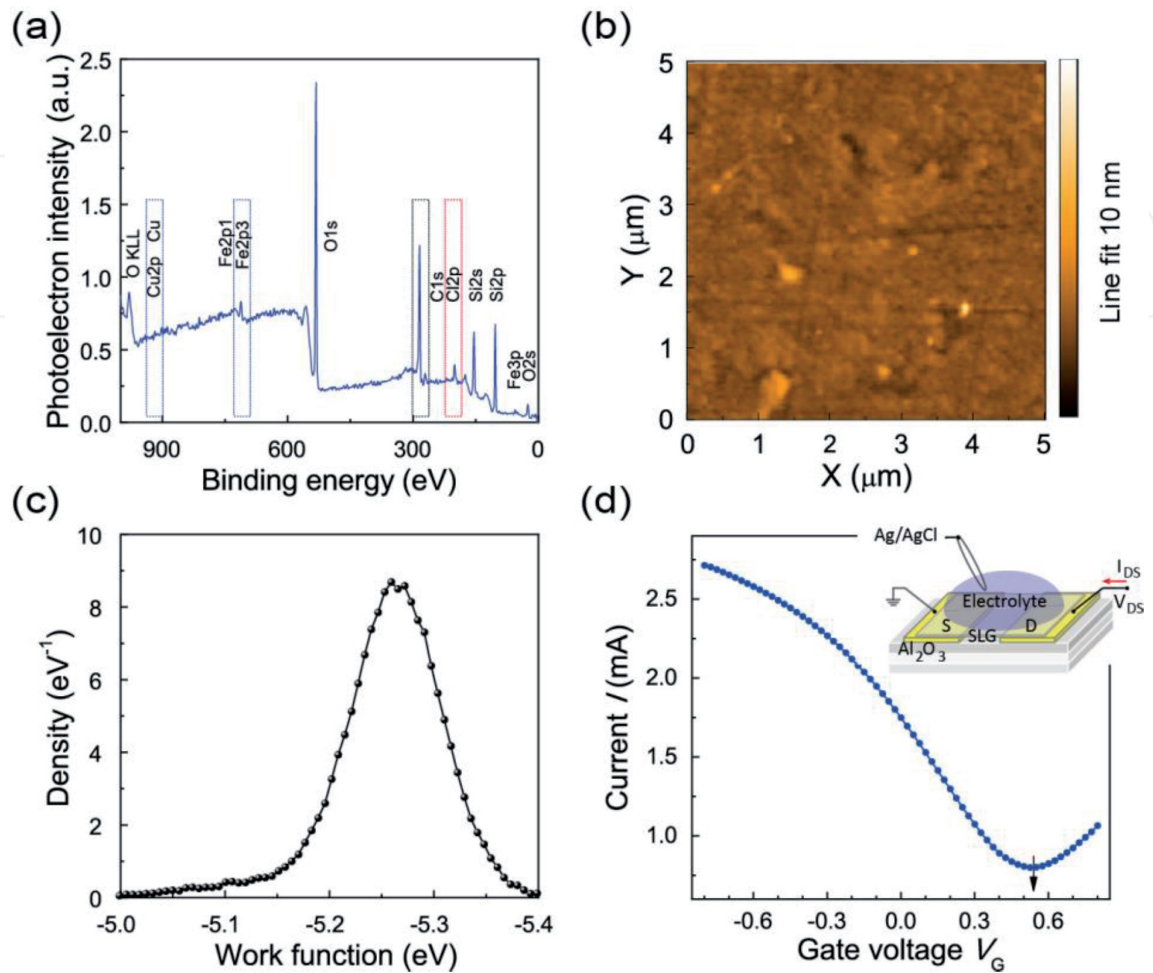

Figure 3.
(a) Wide-scan XPS survey spectra of the studied SLG on a SiO_2/Si substrate. AFM topographic image (5 μm × 5 μm) (b) and corresponding work function distribution (c) of the SLG on the VOLET substrate as measured by KPFM. (d) Transport characteristics of the SLG from liquid-gated lateral Gr-FETs at V_{DS} = −100 mV. The insets show the structure of the liquid-gated lateral Gr-FET with an Ag/AgCl reference electrode in a nonaqueous electrolyte containing ACN and 100 mM of $TBAPF_6$.
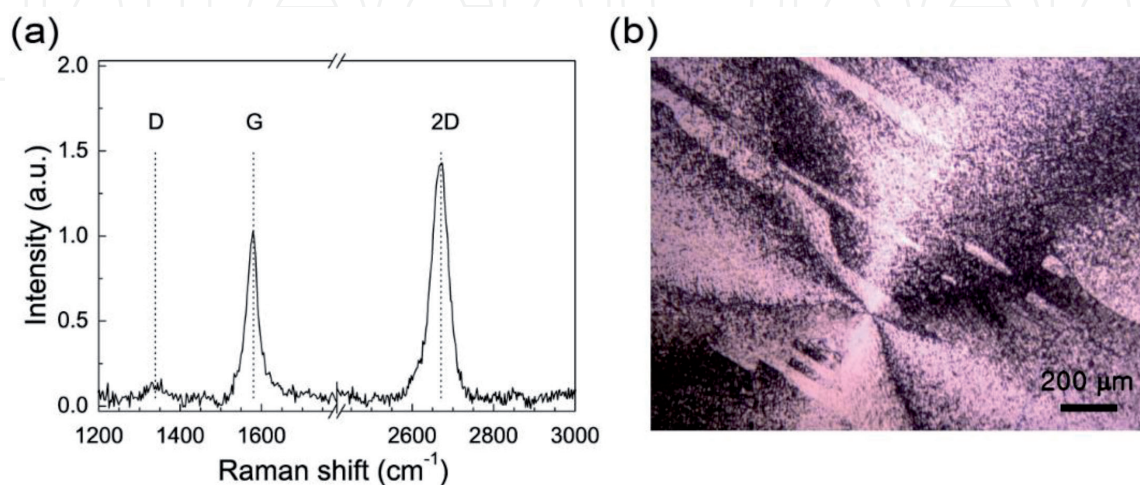

Figure 4.
(a) Raman spectra of the SLG transferred from the Cu foil onto the VOLET substrate. (b) Polarized optical microscope image of a spin-coated layer of commercial nematic liquid crystals on the SLG transferred to the VOLET substrate.

Work function [eV]	Dirac point energy [eV]	Hole mobility [$cm^2 V^{-1} s^{-1}$]	Sheet resistance, [$k\Omega\, square^{-1}$]
5.21	4.89	410	1.20

Table 1.
Summary of the electronic properties of the $FeCl_3$-doped SLG used.

Next, the transport characteristics of the SLG used were observed by assessing a liquid-gated lateral FET with SLG channels, a Gr-FET, as shown in **Figure 3(d)**. The lateral FET substrate was prepared using the VOLET substrate or a heavily doped n-type Si wafer substrate (0.05-ohm cm) with a thermally grown SiO_2 layer (300-nm-thick) as the gate dielectric for the OTFT, together with a laterally pat-terned metal source and drain electrodes consisting of a Cr layer (5.5-nm-thick) and a Au layer (50-nm-thick) formed on the substrate via a vacuum deposition process with a mask. The channel length (L) and width (W) of the FET were 50 μm and 1600 μm, respectively (see inset in **Figure 3(d)**). Regarding the transport characteristics of the SLG studied, a liquid-gated lateral Gr-FET was prepared using an FET substrate with acetonitrile (ACN) with 100 mM of tetrabutylammonium hexafluorophosphate ($TBAPF_6$). The channel of the studied SLG of the Gr-FET was gated through the ACN electrolyte with an Ag/AgCl (3.5 M KCl) reference electrode by sweeping the gate voltages from −0.8 to 0 V and then to +0.8 V with a sweep rate of 30 mV s^{-1} at V_{DS} = 100 mV. In general, the liquid-gate Gr-FET has better transfer characteristics than the conventional back-gate Gr-FET because the liquid gate exhibits higher capacitance than the back gate [49, 50].

For the SLG used here, the Gr-FET showed a clear asymmetrical V-shaped I_{DS}-V_G curve with a charge-neutral gate voltage (or Dirac point, V_{Dirac}) of ~0.54 V/$V_{Ag/AgCl}$. This large positive value of V_{Dirac} clearly indicates that the SLG used is p-type (hole) doped graphene due to the chlorination of graphene by $FeCl_3$ [49]. According to the V_{Dirac} value of the SLG, the energy level of the Dirac point E_D, relative to the vacuum level, can be estimated with regard to the redox potential of a probe material of ferrocene via the following relationship [51]:

$$E_D = \left[-\left(e V_{G,Dirac} - E_{1/2}(Fc/Fc+)\right) - 4.8 \right] \text{ eV.} \tag{2}$$

Here, 4.8 eV is the absolute energy level of the ferrocene and ferrocenium (Fc/Fc+) redox couple below the vacuum energy level, and $E_{1/2(Fc/Fc+)}$ = 0.45 eV [51]. From Eq. (2), the V_{Dirac} value of ~0.54 V/$V_{Ag/AgCl}$ for the SLG gives a Dirac point energy E_D of approximately ~4.89 eV. Note that the E_D value of 4.89 eV is higher than that (~4.49 eV) of epitaxial monolayer graphene [52], also confirm-ing the p-type doping of the SLG. From the transfer characteristics, the carrier (hole) mobility μ of the SLG was also estimated using the relationship [53] of

$$\mu = \left(L / W C_g V_{DS}\right)\left(\Delta I_{DS} / \Delta V_G\right), \tag{3}$$

where C_g is the top-gate capacitance of graphene (~1.9 μF cm^{-2}) [50]. The estimated hole mobility for the SLG was approximately ~410 cm^2 V^{-1} s^{-1}.

For the SLG studied here, Raman spectroscopy was also carried out using a confocal Raman system with a laser source operating at 514.5 nm (~1 mW on sample surface). As shown in **Figure 4(a)**, the Raman spectra of the SLGs studied here have two strong characteristic peaks, a G band at around ~1580–1600 cm^{-1}, due to the E_{2g} vibration of sp^2-bonded carbon atoms, and a 2D band at around ~2644–2665 cm^{-1}, which is a second-order type of vibrational mode caused by the

scattering of phonons at the zone boundary [54, 55]. It can be observed that there are very small disorder-induced D bands around ~1340–1350 cm^{-1}, indicating the sparse formation of sp^3 bonds due to the relatively few defects in the SLGs studied.

From the Raman peak intensities, it was found that the ratios of the integrated Raman intensities of the G band to the 2D band for the FeCl$_3$-doped SLG were in the approximate range of 1.7–1.8, indicating that the SLGs studied here are high-quality monolayer graphene [55]. Moreover, from the peak positions, it was found that while the G and 2D peaks of the intrinsic undoped SLG are positioned at ~1579 cm^{-1} and ~2669 cm^{-1}, respectively, the G and 2D peak positions of the SLG used are correspondingly upshifted to ~1585 cm^{-1} and ~2677 cm^{-1}. Through a comparison of these with other examples in an earlier report of the relationship between the G and 2D peak positions of graphenes [55], it was verified that the SLG used here is p-type doped SLG.

Subsequently, the densities of the defects, the distances between the defects, and the porosities of nano-defects for the SLG were estimated from the ratio of the Raman intensities of the G bands to the D bands, I_D/I_G, as shown in the Raman spectra above. The density of the defects (n_D) and the distances between the defects (L_D) for the SLG, as estimated from the carbon amorphization trajectory ($I_D/I_G \sim 0.117$) [56, 57], were $n_D \sim 3.0 \times 10^{10}$ cm^{-2} and $L_D \sim 32.8$ nm, respectively, corresponding to a porosity of 9.4×10^{-2}%. This result clearly indicates that the SLGs studied here are nonporous high-quality SLGs with a negligible number of porous defects introduced during the synthesis and transfer steps.

Next, for this SLG, polarized optical microscopy was also carried out using SLG covered with commercial nematic liquid crystals (NLCs, Merck LC ZLI-2293) in a crossed polarization state [58]. As shown in **Figure 4(b)**, the polarized optical microscopic image of a spin-coated NLC layer on the SLG shows large graphene domains (with an average radius of the domains >100 μm) in the form of highly uniform optical retardation, in addition to small domains of several hundreds of nanometers in size [59, 60], clearly indicating that the SLG studied here is high-quality graphene with large-area graphene domains.

3. VOLETs with a doped CVD graphene source

3.1 Fabrication of SLG-based VOLETs

Figure 5 presents a schematic illustration of the structure used and the stages of the fabrication of the SLG-based VOLETs (Gr-VOLETs) with an ITO gate separated by an Al$_2$O$_3$ gate dielectric layer, a SLG source, organic channel layers, and an Al drain. The fabrication steps of the Gr-VOLET investigated are described below. To construct the Gr-VOLET, SLG (4 mm by 20 mm) was transferred onto a VOLET substrate, as mentioned above (Steps 1, 2). The source electrode used was FeCl$_3$-doped SLG. Next, organic semiconducting materials were deposited over the SLG source electrode regions; a channel layer of poly(para-phenylene vinylene) copolymer (known as SY, 70-nm-thick) was coated as an emissive channel layer by spin coating (Step 3), after which a 2-nm-thick electron injection layer of CsF and a 80-nm-thick drain electrode of Al were deposited on the top of the SY channel layer in sequence via thermal deposition at a rate of 0.05 nm s^{-1} under a base pressure of less than 2.7×10^{-4} Pa (Step 4). Finally, the fabricated device was encapsulated with an epoxy resin in a glove box. The photograph in **Figure 5** shows the microscopic morphology of the device cross section as observed by field emission scanning electron microscopy (SEM).
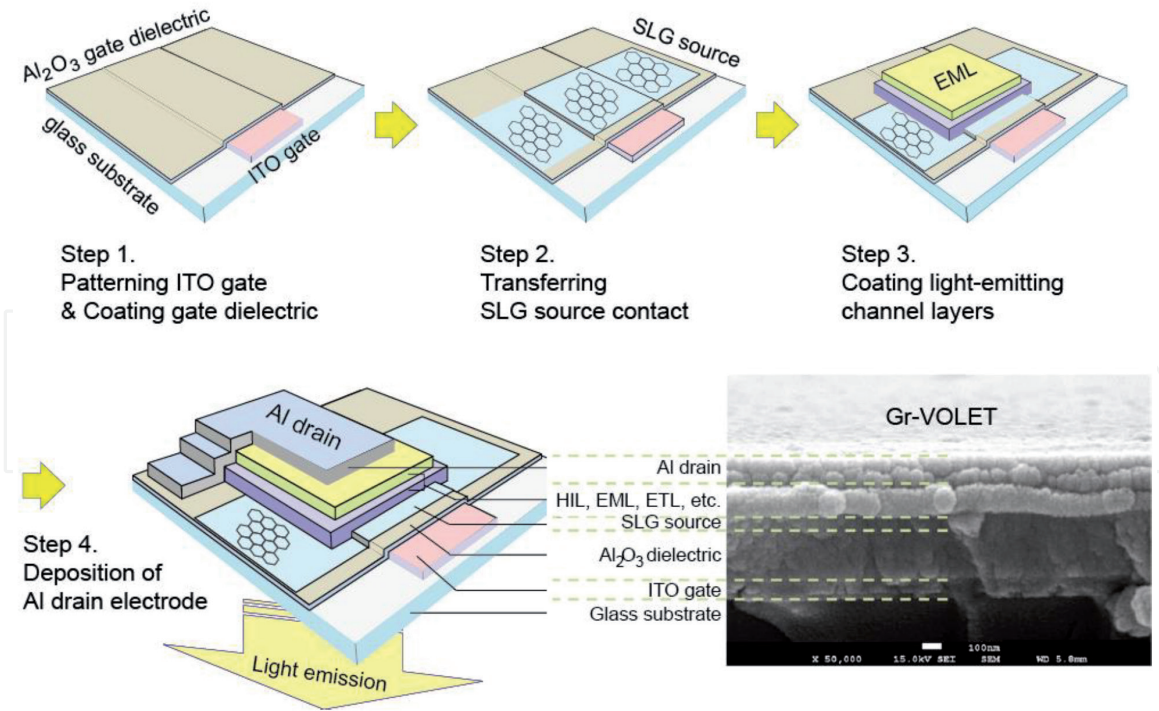
Figure 5.
Schematic illustration of the fabrication steps of a Gr-VOLET and a cross-sectional scanning electron microscopy (SEM) image of the Gr-VOLET with stacked layers of an ITO gate separated with an Al_2O_3 gate dielectric, a SLG source, organic channel layers, and an Al drain.

3.2 Operating characteristics of Gr-VOLETs

The operating characteristics of the Gr-VOLET were observed using a luminance meter in conjunction with two source meters. To operate the Gr-VOLETs, source-drain voltage V_{DS} (= $-V_{SD}$) on the Al drain and gate voltage, V_{GS} (or V_G), were applied with respect to the SLG source contact, held at the ground potential. During the operation of the Gr-VOLET, an electron injection occurs from the Al drain into the SY channel layer, and the hole injection from the SLG source to the SY channel layer can be modulated by controlling the gate voltage V_{GS} (or V_G), as discussed below.

Figure 6 shows the EL light emissions of a Gr-VOLET operating under different V_G values with a fixed V_{SD} of 3.8 V. As shown in **Figure 6(b)**, the EL light emission is uniform and bright (in the on-state) and evenly dark (off-state) over the entire surface of the active area for negative and positive V_G values, respectively. Hence, V_G essentially influences the radiative recombination process in the emissive channel layers.
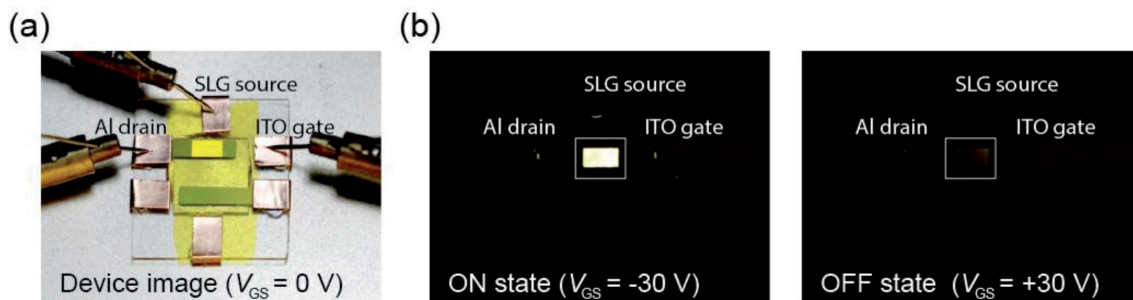

Figure 6.
EL light emission from a Gr-VOLET for different gate voltages, V_{GS}, for a given source-drain voltage, V_{SD}, of 3.8 V in bright (a) and dark (b) conditions (active area: 4 mm × 2 mm, white squares).

The output current and luminance characteristics of the Gr-VOLET were investigated as described below. For comparative purposes, the diode characteristics of the Gr-VOLET were also observed with the gate electrodes isolated from the external circuits (Gr-OLED). As shown in **Figure 7**, the current density-voltage (J_{SD}-V_{SD}) characteristics and luminance-voltage (L-V_{SD}) characteristics of the Gr-VOLET present the following key features: (i) the J_{SD}-V_{SD} characteristics are similar to the diode characteristics, as is generally observed in vertical organic FETs due to the short channel lengths [61]. (ii) Similar behaviors were observed in the L-V_{SD} characteristics; (iii) for a given V_{SD}, both J_{SD} and L increase with a decrease in V_G, even at low V_{SD} values, indicating that current modulation by V_G can change the EL emission brightness. Thus, the V_G dependent turn-on voltage, V_{onset}, can be reduced to well below V_{onset} of the Gr-OLED, and (iv) both J_{SD} and L also depend on the direction of change of V_G, that is, upward or downward, implying hysteretic behavior.

Interestingly, as shown in **Figure 7**, at V_G = −40 V, the Gr-VOLET with the doped SLG source exhibits high device performance, superior to that of the Gr-OLED, indicating an improved and balanced charge injection from the SLG source for negative V_G values. Conversely, at V_G = +40 V, J_{SD} and L of the Gr-VOLET are much lower, due to the switching off effect of the hole injections from the SLG source. The highest values of the peak on/off ratios for J_{SD} and L were ~10^2 and ~10^4, respectively, at V_G = ±40 V. Thus, the gate-bias-induced modulation effect of Gr-VOLET is shown to be quite efficient.

Next, the device performance, AR_{eff}, and PPC, of the Gr-VOLET were estimated in the on-state in comparison with a control OLED fabricated using an identical process on an ITO anode (ITO-OLED) (**Figure 8**). As shown in **Figure 8**, the Gr-VOLET exhibits EL luminance higher than that of the control OLED (ITO/SY/CsF/Al) in the V_{SD} < 4.0 V region. Moreover, the Gr-VOLET was shown to be more efficient than the control OLED (**Figure 8(c)**). For instance, at an EL luminance level of 500 cd m^{-2}, the Gr-VOLET emitted EL light with a current efficiency, η_C, of 7.13 cd A^{-1}, which is approximately 154% of the η_C result (4.64 cd A^{-1}) for the control ITO-OLED. Thus, the AR_{eff} value of the Gr-VOLET can be estimated to be 154% due to its full surface emission, just like the OLED. Thus, it is clear that the Gr-VOLET has a greatly enhanced AR_{eff} compared to other reported devices (**Table 2**). This result offers another substantial advantage: given the level of AR_{eff}, the brightness of the device can be maintained under a lower J_{SD}, providing a longer device lifetime
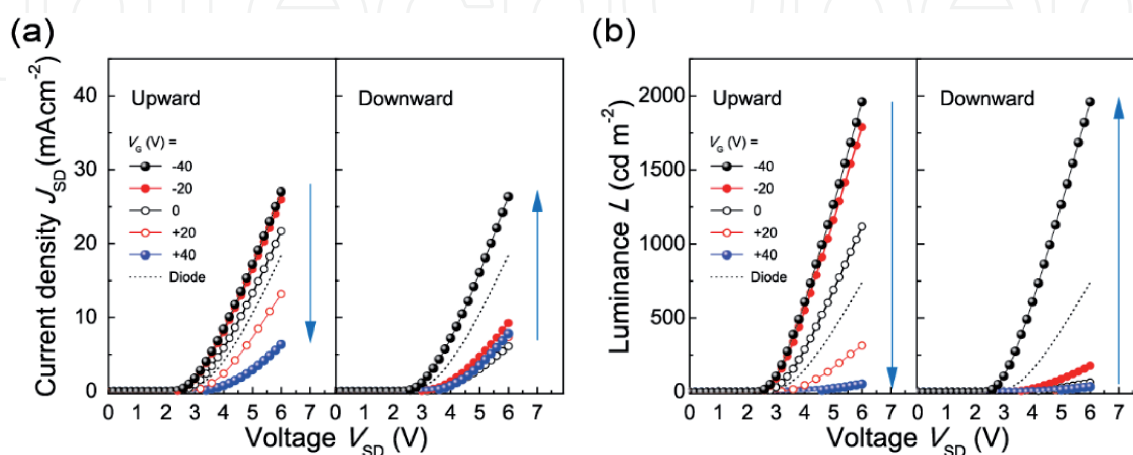

Figure 7.
Gate-voltage (V_G)-dependent current density-voltage (J_{SD}-V_{SD}) (a) and luminance-voltage (L-V_{SD}) (b) characteristics of a Gr-VOLET with a FeCl$_3$-doped SLG source for upward and downward changes in V_G. For comparison, the characteristics of a Gr-OLED (i.e., gate-disconnected Gr-VOLET) are also shown (dotted curves, OLED operations).
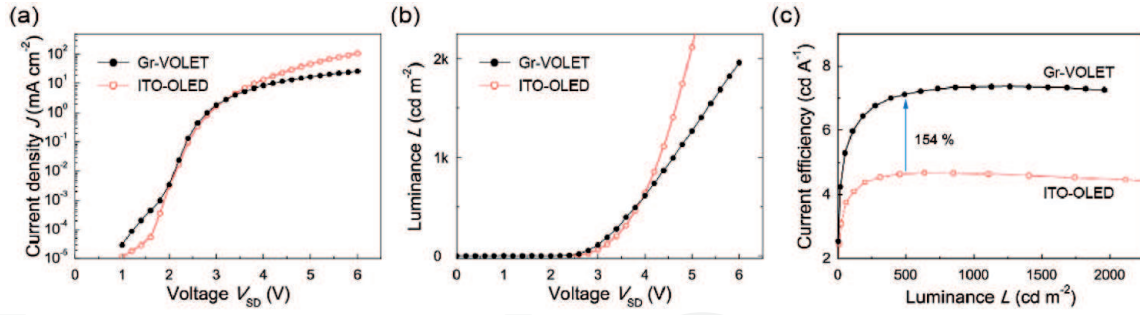
Figure 8.
J-V (a), L-V (b), and η_C-L (c) comparisons of the Gr-VOLET in the bright on-state ($V_G = -40$ V) with its ITO-based control OLED (ITO-OLED). Note that ITO-OLED = (ITO/SY/CsF/Al).

Devices	Reference	Source type	AR_{eff} [%]	PPC [%]
TFT + OLED	[15]			53
MIS-OLET	[19]			51
CNT-VOLET[a]	[32]	Porous CNT networks	98	6.2
Gr-VOLET	This work [49]	FeCl$_3$-doped SLG	154	5.2

[a]*Reference devices used the green phosphorescent emitter Ir(ppy)$_3$.*

Table 2.
Comparison of the effective aperture ratio, AR_{eff}, and parasitic power consumption, PPC, for various devices at a luminance level of 500 cd m^{-2}.

[62]. It is noteworthy that η_C (7.13 cd A^{-1}) for the Gr-VOLET was approximately 1.4 times higher than η_C (5.17 cd A^{-1}) of the ITO-OLED, possessing the optimized HIL of PEDOT:PSS. Thus, it is clear that the SLG source in the Gr-VOLET provides amplification of the emission and current efficiency, although further optimization of the electrodes is still possible.

Next, the PPC of the Gr-VOLET was deduced, which achieved luminance of 500 cd m^{-2} at V_{SD} = 3.82 V with an AR_{eff} rate of 154%, as discussed above. For the control ITO-OLED to emit a luminous flux through an aperture while transmitting 154% of its light, thereby matching the Gr-VOLET, it must emit 324 cd m^{-2}, requiring an applied voltage of 3.62 V. This indicates that 0.2 V of the V_{SD} (3.82 V) for the Gr-VOLET was dropped through its embedded transistor element, leading to a considerably reduced PPC of only 5.2%. This is much lower than that (6.2%) of the previous CNT-VOLET and the levels (>50%) for a TFT-OLED and a MIS-OLET (**Table 2**) [19, 32].

3.3 Charge injection process at SLG sources

At this point, our investigation turns to the hole injection mechanism at the interface between the SY channel layer and the SLG source. To be injected across the interface (SLG/SY), the holes must overcome the barrier height at the interface either via thermionic emission or tunneling processes [63–68]. **Figure 9(a)** shows examples of Fowler-Nordheim (F-N) curves [63–67] for the Gr-VOLET at various V_Gs during upward changes in V_G. All of the curves show two different hole injection processes with transition voltages (V_Ts), at which the injection mechanism changes to tunneling from Schottky thermionic emission [63–68]. In the figure, it is interesting to note that V_G affects both the Schottky thermionic emission and tunneling, indicating that V_T strongly depends on V_G. It is also noteworthy that because EL emission of the Gr-VOLETs occurs when $V_{SD} > V_{onset}$ ($V_{onset} > V_T$), the main
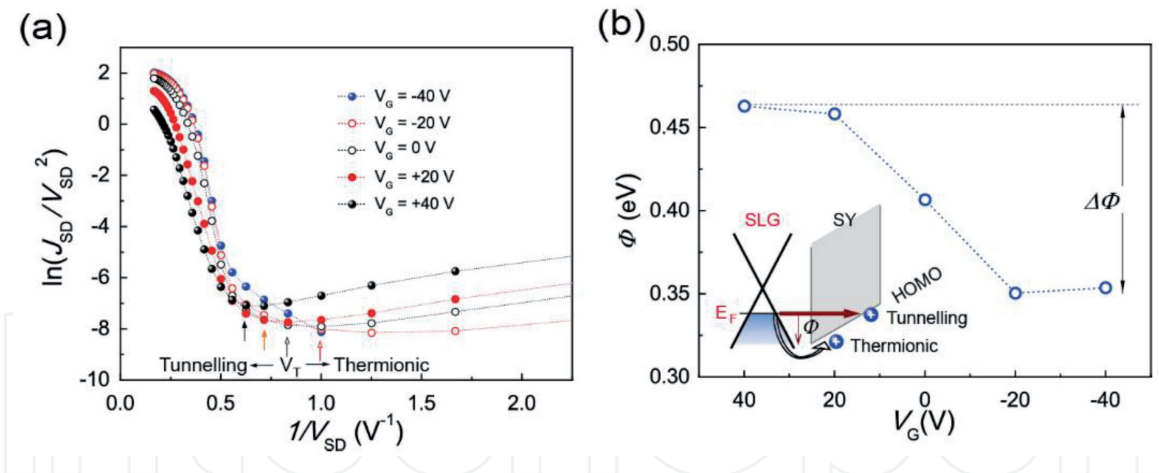
Figure 9.
(a) Fowler-Nordheim plots of the Gr-VOLET with the SLG source with various V_G values for upward V_G changes. (b) Gate-bias-modulated hole tunneling barrier height, Φ, extracted from the curve fittings in the hole-dominant regimes. The inset shows a schematic energy band diagram for the thermionic emission and tunneling at the interface between the SLG and the SY layer along the normal direction of the interface. Φ denotes the interface potential barrier height between the SLG and the SY channel layer.

hole injection process for EL emission is the tunneling injection in the Gr-VOLETs. According to the modified tunneling current model [70], the tunneling current density (J) of a single charge carrier through a triangular barrier at a polymer/metal junction is related to the potential barrier height (Φ) and the temperature (T),

$$\ln\left(J/V^2\right) = -P_1/V + \ln\left(P_2/V\right) - \ln\left[\sin\left(P_3/V\right)\right],$$
$$\text{with} \Phi = (2/3)\,\pi\,k_B T\,(P_1/P_3), \tag{4}$$

where k_B is the Boltzmann constant and P_i are parameters related to Φ. This relationship allows the F-N plots to be analyzed, and the potential barrier heights Φ at the SLG/SY interface between the Fermi level of SLG and the highest occupied molecular orbital (HOMO) level of the SY channel layer (~5.3 eV) [22] to be obtained (**Figure 9(b)**). As shown in the figure, the SLG/SY interface exhibited strong gate-bias-induced Φ modulation ($\Delta\Phi$) along the direction normal to the SLG/SY interface; that is, $\Delta\Phi$ at $V_G = \pm40$ V was approximately 0.11 eV, leading to the effective modulation of the device performance of the Gr-VOLET tested here. Note that tunneling at the SLG/SY interface is the major process of hole injection, being responsible for the radiative recombinations of electron-hole pairs. Thus, the analysis of the tunneling process described above provides clear evidence that the Gr-VOLET operates based on vertical barrier height modulation along the direction normal to the SLG source surface (i.e., parallel to the direction of gate field), in contrast to the CNT-VOLET devices based on lateral modulation of Schottky barrier height along the horizontal direction on the CNT source surface (i.e., perpendicular to the direction of gate field) [31, 32], and differently from conventional graphene-based barristors that operate via modulation of the Schottky thermionic injection [69, 70].

The observations above show the working principle of the Gr-VOLET, as illustrated in the energy-level diagrams in **Figure 10**. At a given V_{SD}, a positive gate voltage induces an upward shift of the SLG Fermi level in a direction that increases the Φ, resulting in reduced hole tunneling injections into the HOMO level of the channel layer (SY). In contrast, a negative gate voltage induces a downward shift of the SLG Fermi level, decreasing Φ significantly (enhancing tunneling) and hence allowing increased hole injections and improved EL performance. Thus, together with the band-bending effect [31], the main operating mechanism of the Gr-VOLET
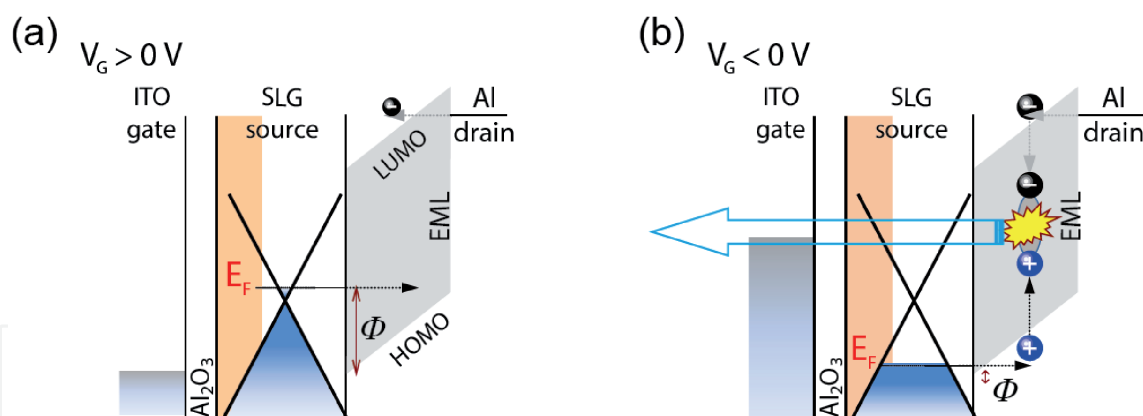
Figure 10.
Energy-level diagrams of the Gr-VOLET for high (a) and low Φs (b) at two distinct values of V_G and a given V_{SD}. Φ depicts the tunneling barrier height for the hole injection. E_F: Fermi energy level of the SLG source used.

is energy band matching, with charge balance achieved even without a HIL through gate voltage-induced modulation of the hole carrier tunneling injection at the p-type doped SLG source with $FeCl_3$.

In addition, notable instances of hysteresis were clearly observed, as shown above. Thus, bistable-like switching operations of a Gr-VOLET can allow novel applications for simple and inexpensive driving schemes together with low power consumption. However, this hysteresis effect may become an issue when attempting to realize high-quality grayscale outcomes and should be carefully, therefore, controlled when preparing the dielectric layer.

3.4 Inkjet-printing arrays of Gr-VOLET micro-pixels

Next, we turn our attention to a micro-pixel fabrication process for the Gr-VOLET using the inkjet-printing technique, as commonly used in solution-processable OLEDs [39, 71, 72]. Here, the inkjet technique used is based on the deposition of a small solvent drop onto an insulator layer, which can be easily redissolved and preferentially redeposited at the edge of the sessile drop (the contact line of the solvent drop), resulting in the formation of a via-hole with the shape of a crater, that is inkjet-etching [39].

To investigate the in situ formation of micro Gr-VOLET pixels created by means of inkjet-etching, an insulating polymer of poly(4-vinylpyridine) (P4VP) was introduced as a via-forming material, as P4VP is a hydrophilic polymer that dissolves in dimethyl formamide (DMF), toluene, chloroform, in lower alcohols, and in aqueous mineralic acids [71]. To fabricate a via-hole forming layer, a solution of P4VP with isopropanol (IPA) was spin-coated on top of the light-emitting channel layer of SY pre-coated onto a Gr-VOLET substrate (VOLET substrate/SLG/SY/P4VP). For micro-patterning, an etching solvent of chloroform for P4VP was inkjet-printed on top of the SY/P4VP layers (**Figure 11(a)**). This inkjet-printed solvent drop of chloroform can dissolve the P4VP layer, and the capillary flow of the solvent pushes the dissolved P4VP from the center to the contact line of droplet due to the coffee ring effect [39, 72–74], resulting the formation of the via-hole through the P4VP layer. Thus, after the deposition of even a single solvent droplet (~150 pL per droplet) on a 30-nm-thick P4VP film, the P4VP polymers are removed from the printed position and completely etched, forming via-holes through the P4VP layer, of which the inner and outer diameters are ~90 μm and ~120 μm, respectively, and finally uncovering the surface of the underlying SY layer. These P4VP via-holes on the light-emitting SY layer act as micro-patterned pixel openings
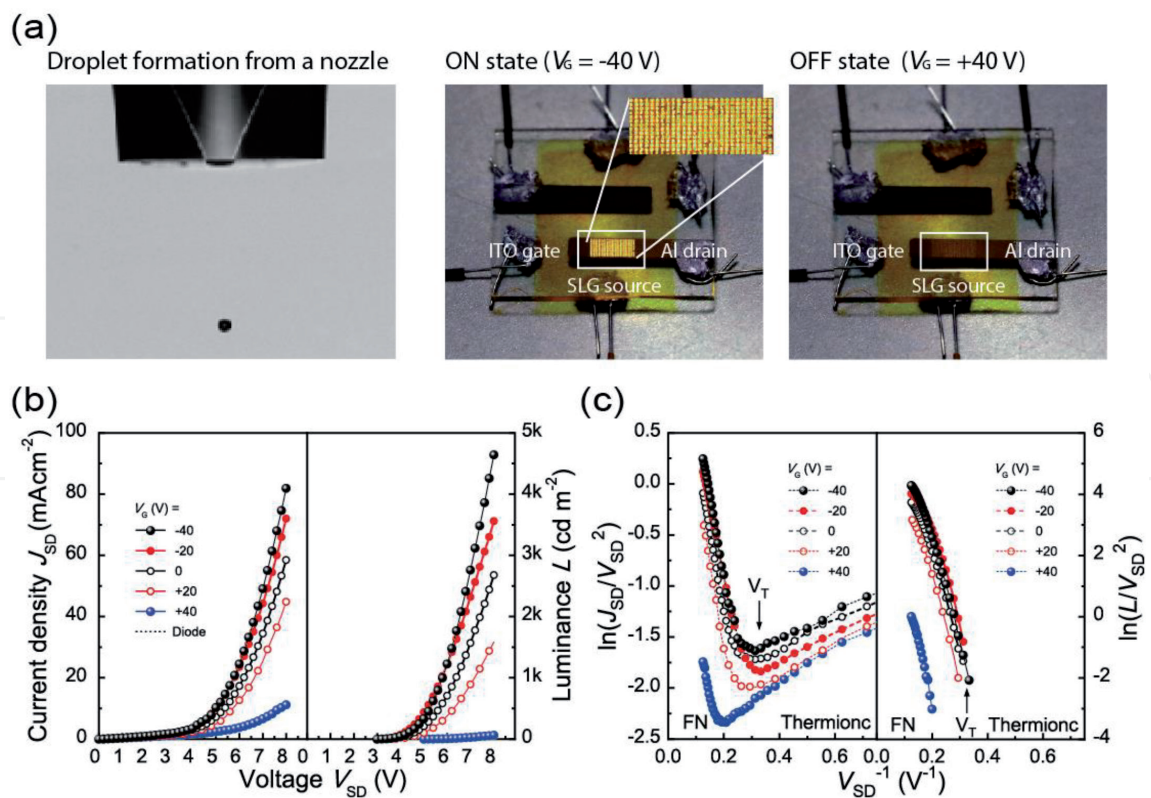
Figure 11.
(a) Left: A photographic image of a single drop of solvent ejected from an inkjet nozzle for drop formation. Right: Light emission from inkjet-printed Gr-VOLET pixels (white squares) for two different gate voltages V_Gs, at a fixed $V_{SD} = 4.0$ V. (b) Gate-voltage (V_G)-dependent current density-voltage (J_{SD}-V_{SD}) (left) and luminance-voltage (L-V_{SD}) (right) characteristics of the inkjet-printed Gr-VOLET pixels for various upward V_G changes. (c) Fowler-Nordheim plots, $\ln(J_{SD}/V_{SD}^2)$ vs. $1/V_{SD}$ (left) and $\ln(L/V_{SD}^2)$ vs. $1/V_{SD}$ (right) for the inkjet-printed Gr-VOLET pixels at various V_G values.

for the light-emitting active areas of the Gr-VOLETs. Then, to complete the device of an array of micro Gr-VOLETs, the CsF/Al/Ag cathode is deposited following the procedure described in Section 3.1.

Figure 11(a) also presents the switching behavior of EL light emissions from the array of micro Gr-VOLET pixels for two different gate voltages, V_Gs, at a fixed V_{SD} of 4.0 V. The photographic images show that only the isolated micro-patterned micro-pixel areas in contact with the SY layer of the Gr-VOLET pixels can emit EL light with a width of 85 μm, similar to the dimensions of the via-hole opening (90 μm). Note that the different solubility characteristics between the P4VP and SY polymers prevents any solvent erosion of the SY layer, as expected. As also clearly shown in the figure, the EL light emission from the micro Gr-VOLET pixels with a fixed droplet spacing of ~140 μm (~180 dpi) is highly bright (on-state) and dark (off-state) over the entire active area of the pixels for negative (−40 V) and positive values of V_G (+40 V), respectively. Hence, V_G clearly controls the radiative recombination process in the emissive pixel areas.

Next, the output characteristics of the inkjet-printed Gr-VOLET pixels were investigated. As shown in **Figure 11(b)**, the J_{SD}-V_{SD} and L-V_{SD} characteristics of the inkjet-printed Gr-VOLET pixels present features similar to those of the spin-coated Gr-VOLET (**Figure 7**). For example, at $V_G = −40$ V, the luminance reaches $L \sim 1200$ cd m^{-2} with a current efficiency of ~5.0 cd/A at $V_{SD} = 6.0$ V ($V_{onset} = 3.0$ V). In contrast, at $V_G = +40$ V, J_{SD} and L are greatly suppressed due to the switching off effect of the injection of holes from the SLG source, resulting in a peak on/off ratio of L of approximately 10^3 at $V_G = \pm40$ V. **Figure 11(c)** presents F-N plots of the micro Gr-VOLET pixels for various V_Gs. As also shown

in the figure, the negative slopes of the F-N plots clearly confirm that tunneling injection process is the major charge injection process for the light emission, being responsible for radiative recombinations of electron–hole pairs in the inkjet-printed Gr-VOLET pixels.

4. Conclusions

In summary, herein, graphene-based VOLETs have been explored, consisting of a nonporous, homogeneous, and p-doped SLG source with $FeCl_3$, an Al drain, and an emissive channel layer for efficient switching of the device performance using the gate voltage. Initially, we investigated transferred CVD SLG, which was used as the source electrode. It was found that the SLG used here was unintended p-doped SLG, exhibiting a Dirac point energy of ~4.9 eV and a work function of 5.2 eV with a shift of the Fermi level from the Dirac point and high hole mobility. It is shown that the high device performance capabilities of SLG-based VOLETs were mainly due to the p-doping effects, which were estimated quantitatively and analyzed based on the energy levels of the SLGs. It is also shown that low-drain-voltage operations and increased brightness with a high luminance on/off ratio (~10^4) can be achieved even at high brightness for the Gr-VOLET without any HIL. Moreover, the current efficiency and effective aperture ratio of the Gr-VOLET were at least 150% higher than those of a control OLED, with low parasitic power consumption of 5%. These significant improvements of the device performance can be attributed to the gate-bias-induced modulation of the hole tunneling injection from the $FeCl_3$-doped SLG source into the emissive channel layer. Further, the feasibility of the simple fabrication process of micro Gr-VOLET pixels, that is, the inkjet-printing technique, was also proven.

The foregoing results demonstrate the notable device performance of the Gr-VOLET with graphene source, indicating considerable promise with respect to the development of high-performance VOLETs. The advances afforded by the Gr-VOLET with reliable switching performance, even at high luminance levels, clearly show its effective light-emitting transistor functionality and make it a feasible candidate for development of new voltage-driving light-emitting devices and/or highly integrated organic optoelectronics. Finally, it will be possible to apply advanced material layers to these Gr-VOLETs, which could lead to more efficient devices that operate even at low voltage levels, enabling the development of inexpensive, large-area, fast, and high-performance AM displays. Further improvements and characterizations are in progress and will be published elsewhere.

Acknowledgements

Author details

Byoungchoo Park*, Won Seok Lee, Seo Yeong Na, Jaewoo Park and In-Gon Bae
Department of Electrical and Biological Physics, Kwangwoon University, Seoul,
Republic of Korea

*Address all correspondence to: bcpark@kw.ac.kr

IntechOpen

References

[1] Tang CW, VanSlyke SA. Organic electroluminescent diodes. Applied Physics Letters. 1987;**51**:913-915. DOI: 10.1063/1.98799

[2] Burroughes JH, Bradley DDC, Brown AR, Marks RN, Mackay K, Friend RH, et al. Light-emitting diodes based on conjugated polymers. Nature. 1990;**347**:539-541. DOI: 10.1038/348352a0

[3] Yu G, Gao J, Hummelen JC, Wudl F, Heeger AJ. Polymer photovoltaic cells: Enhanced efficiencies via a network of internal donor-acceptor heterojunctions. Science. 1995;**270**: 1789-1791. DOI: 10.1126/science

[4] Chen HY, Hou J, Zhang S, Liang Y, Yang G, Yang Y, et al. Polymer solar cells with enhanced open-circuit voltage and efficiency. Nature Photonics. 2009;**3**: 649-653. DOI: 10.1038/nphoton.2009.192

[5] Sirringhaus H, Brown PJ, Friend RH, Nielsen MM, Bechgaard K, Langeveld-Voss BMW, et al. Two-dimensional charge transport in self-organized, high-mobility conjugated polymers. Nature. 1999;**401**:685-688. DOI: 10.1038/44359

[6] Bucella SG, Luzio A, Gann E, Thomsen L, McNeill CR, Pace G, et al. Macroscopic and high-throughput printing of aligned nanostructured polymer semiconductors for MHz large-area electronics. Nature Communications. 2015;**6**:8394. DOI: 10.1038/ncomms9394

[7] Baldo MA, O'Brien DF, You Y, Shoustikov A, Sibley S, Thompson ME, et al. Highly efficient phospho-rescent emission from organic electroluminescent devices. Nature. 1998;**395**:151-154. DOI: 10.1038/25954

[8] Wang Q, Ding J, Ma D, Cheng Y, Wang L, Jing X, et al. Harvesting excitons via two parallel channels for efficient white organic LEDs with nearly 100% internal quantum efficiency: Fabrication and emission-mechanism analysis. Advanced Functional Materials. 2009;**19**:84-95. DOI: 10.1002/adfm.200800918

[9] Gu G, Forrest SR. Design of flat-panel displays based on organic light-emitting devices. IEEE Journal of Selected Topics in Quantum Electronics. 1998;**4**:83-99. DOI: 10.1109/2944.669473

[10] Shinar J, Shinar R. Organic light-emitting devices (OLEDs) and OLED-based chemical and biological sensors: An overview. Journal of Physics D: Applied Physics. 2008;**41**:133001. DOI: 10.1088/0022-3727/41/13/133001

[11] Lin YY, Gundlach DI, Nelson SF, Jackson TN. Pentacene-based organic thin-film transistors. IEEE Transactions on Electron Devices. 1997;**44**:1325-1331. DOI: 10.1109/16.605476

[12] Brody TP, Luo FC, Szepesi ZP, Davies DHA. A 6 × 6-in 20-lpi electroluminescent display panel. IEEE Transactions on Electron Devices. 1975;**22**:739-748. DOI: 10.1109/T-ED.1975.18214

[13] Nam WJ, Kim CY, Lee JH, Park SG, Han MK. 44.3: High-aperture ratio AMOLED pixel design employing VDD line elimination for reducing OLED current density. SID Symposium Digest of Technical Papers. 2005;**36**:1456-1459. DOI: 10.1889/1.2036282

[14] Nag M, Obata K, Fukui Y, Myny K, Schols S, Vicca P, et al. 20.1: Flexible AMOLED display and gate-driver with self-aligned IGZO TFT on plastic foil. In: SID Symposium Digest of Technical Papers. Vol. 45. 2014. pp. 248-251. DOI: 10.1002/j.2168-0159.2014.tb00068.x

[15] Ohta S, Chuman T, Miyaguchi S, Satoh H, Tanabe T, Okuda Y, et al.

Active matrix driving organic light-emitting diode panel using organic thin-film transistors. Japanese Journal of Applied Physics. 2005;**44**:3678-3681. DOI: 10.1143/jjap.44.3678

[16] Perumal A, Fröbel M, Gorantla S, Gemming T, Lüssem B, Eckert J, et al. Novel approach for alternating current (AC)-driven organic light-emitting devices. Advanced Functional Materials. 2012;**22**:210-217. DOI: 10.1002/adfm.201100747

[17] Kudo K, Tanaka S, Iizuka M, Nakamura M. Fabrication and device characterization of organic light emitting transistors. Thin Solid Films. 2003;**438**:330-333. DOI: 10.1016/s0040-6090(03)00751-x

[18] Park B, Takezoe H. Enhanced luminescence in top-gate-type organic light-emitting transistors. Applied Physics Letters. 2004;**85**:1280-1282. DOI: 10.1063/1.1784044

[19] Nakamura K, Hata T, Yoshizawa A, Obata K, Endo H, Kudo K. Improvement of metal–insulator–semiconductor-type organic light-emitting transistors. Japanese Journal of Applied Physics. 2008;**47**:1889-1893. DOI: 10.1143/jjap.47.1889

[20] Santato C, Capelli R, Loi MA, Murgia M, Cicoira F, Roy VAL, et al. Tetracene-based organic light-emitting transistors: Optoelectronic properties and electron injection mechanism. Synthetic Metals. 2004;**146**:329-334. DOI: 10.1016/j.synthmet.2004.08.028

[21] Muccini M. A bright future for organic field-effect transistors. Nature Materials. 2006;**5**:605-613. DOI: 10.1038/nmat1699

[22] Muhieddine K, Ullah M, Pal BN, Burn P, Namadas EB. All solution-processed, hybrid light emitting field-effect transistors. Advanced Materials.

2014;**26**:6410-6415. DOI: 1002/adma.201400938

[23] Capelli R, Toffanin S, Generali G, Usta H, Facchetti A, Muccini M. Organic light-emitting transistors with an efficiency that outperforms the equivalent light-emitting diodes. Nature Materials. 2010;**9**:496-503. DOI: 10.1038/nmat2751

[24] Ullah M, Armin A, Tandy K, Yambem SD, Burn PL, Meredith P, et al. Defining the light emitting area for displays in the unipolar regime of highly efficient light emitting transistors. Scientific Reports. 2015;**5**:8818. DOI: 10.1038/srep08818

[25] Muhieddine K, Ullah M, Maasoumi F, Burn PL, Namdas EB. Hybrid area-emitting transistors: Solution processable and with high aperture ratios. Advanced Materials. 2015;**27**:6677-6682. DOI: 10.1002/adma.201502554

[26] Hu Y, Lin J, Song L, Lu Q, Zhu W, Liu X. Vertical microcavity organic light-emitting field-effect transistors. Scientific Reports. 2016;**6**:23210. DOI: 10.1038/srep23210

[27] Zhang C, Chen P, Hu W. Organic light-emitting transistors: Materials, device configurations, and operations. Small. 2016;**12**:1252-1294. DOI: 10.1002/smll.201502546

[28] Liu CF, Liu X, Lai WY, Huang W. Organic light-emitting field-effect transistors: Device geometries and fabrication techniques. Advanced Materials. 2018;**30**:1802466. DOI: 10.1002/adma.201802466

[29] Muccini M, Toffanin S. Handbook of Organic Light-Emitting Transistors: Towards the Next Generation Display Technology. 1st ed. Hoboken, New Jersey: John Wiley & Sons, Inc.; 2016. 277 p. DOI: 10.1002/9781119189978

[30] Nakayama K, Pu YJ, Kido J. Surface-light-emitting transistors based on vertical-type metal-base organic transistors. Journal of the Society for Information Display. 2011;**19**:602-607. DOI: 10.1889/jsid19.9.602

[31] Liu B, McCarthy MA, Yoon Y, Kim DY, Wu Z. So F, et al. carbon-nanotube-enabled vertical field effect and light-emitting transistors. Advanced Materials. 2008;**20**:3605-3609. DOI: 10.1002/adma.200800601

[32] McCarthy MA, Liu B, Donoghue EP, Kravchenko I, Kim DY. So F, et al. low-voltage, low-power, organic light-emitting transistors for active matrix displays. Science. 2011;**332**:570-573. DOI: 10.1126/science.1203052

[33] Liu B, McCarthy MA, Iheanacho B, Wong WS, Rinzler AG. Recent developments of carbon nanotube enabled vertical organic light emitting transistors for OLED displays. SID Symposium Digest of Technical Papers. 2013;**44**:251-253. DOI: 10.1002/j.2168-0159.2013.tb06192.x

[34] McCarthy MA, Liu B, Cheney DJ, Lemaitre MG, Jayaraman R, Mativenga M, et al. QVGA AMOLED displays using the carbon nanotube enabled vertical organic light emitting transistor. SID Symposium Digest of Technical Papers. 2016;**47**:1796-1798. DOI: 10.1002/sdtp.11071

[35] Lee B, Chen Y, Cook A, Zakhidov A, Podzorov V. Stable doping of carbon nanotubes via molecular self-assembly. Journal of Applied Physics. 2014;**116**:144503. DOI: 10.1063/1.4897550

[36] Geim AK, Novoselov KS. The rise of graphene. Nature Materials. 2007;**6**:183-191. DOI: 10.1038/nmat1849

[37] Ando T. The electronic properties of graphene and carbon nanotubes. NPG Asia Materials. 2009;**1**:17-21. DOI: 10.1038/asiamat.2009.1

[38] Bae S, Kim H, Lee Y, Xu X, Park JS, Zheng Y, et al. Roll-to-roll production of 30-inch graphene films for transparent electrodes. Nature Nanotechnology. 2010;**5**:574-578. DOI: 10.1038/nnano.2010.132

[39] Zhang Y, Liua C, Whalley DC. The impact of substrate temperature on the size and aspect ratio of inkjet-dissolved via holes in thin poly(4-vinyl phenol) dielectric layers. Applied Physics Letters. 2013;**102**:103303-103305. DOI: 10.1063/1.4795447

[40] Park B, Huh JN, Lee WS, Bae IG. Simple and rapid cleaning of graphenes with a 'bubble-free' electrochemical treatment. Journal of Materials Chemistry C. 2018;**6**:2234-2244. DOI: 10.1039/c7tc05695h

[41] Reina A, Jia X, Ho J, Nezich D, Son H, Bulovic V, et al. Large area, few-layer graphene films on arbitrary substrates by chemical vapor deposition. Nano Letters. 2009;**9**:30-35. DOI: 10.1021/nl801827v

[42] Li X, Cai W, An J, Kim S, Nah J, Yang D, et al. Large-area synthesis of high-quality and uniform graphene films on copper foils. Science. 2009;**324**:1312-1314. DOI: 10.1126/science.1171245

[43] Zhang Y, Zhang L, Zhou C. Review of chemical vapor deposition of Graphene and related applications. Accounts of Chemical Research. 2013;**46**:2329-2339. DOI: 10.1021/ar300203n

[44] Suk JW, Kitt A, Magnuson CW, Hao Y, Ahmed S, An J, et al. Transfer of CVD-grown monolayer graphene onto arbitrary substrates. ACS Nano. 2011;**5**:6916-6924. DOI: 10.1021/nn201207c

[45] Li X, Zhu Y, Cai W, Borysiak M, Han B, Chen D, et al. Transfer of large-area graphene films for high-performance transparent conductive

electrodes. Nano Letters. 2009;**9**:4359-4363. DOI: 10.1021/nl902623y

[46] Vinogradov NA, Simonov KA, Generalov AV, Vinogradov AS, Vyalikh DV, Laubschat C, et al. Controllable p-doping of graphene on Ir(1 1 1) by chlorination with FeCl$_3$. Journal of Physics Condensed Matters. 2012;**24**:314202. DOI: 10.1088/0953-8984/24/31/314202

[47] Yu YJ, Zhao Y, Ryu S, Brus LE, Kim KS, Kim P. Tuning the graphene work function by electric field effect. Nano Letters. 2009;**9**:3430-3434. DOI: 10.1021/nl901572a

[48] Panchal V, Pearce R, Yakimova R, Tzalenchuk A, Kazakova O. Standardization of surface potential measurements of graphene domains. Scientific Reports. 2013;**3**:2597. DOI: 10.1038/srep02597

[49] Park B, Lee WS, Na SY, Huh JN, Bae IG. Full-surface emission of graphene-based vertical-type organic light-emitting transistors with high on/off contrast ratios and enhanced efficiencies. Scientific Reports. 2019;**9**:6328. DOI: 10.1038/s41598-019-42800-y

[50] Ohno Y, Maehashi K, Yamashiro Y, Matsumoto K. Electrolyte-gated graphene field-effect transistors for detecting pH and protein adsorption. Nano Letters. 2009;**9**:3318-3322. DOI: 10.1021/nl901596m

[51] Padhy H, Huang JH, Sahu D, Patra D, Kekuda D, Chu CW, et al. Synthesis and applications of low-bandgap conjugated polymers containing phenothiazine donor and various benzodiazole acceptors for polymer solar cells. Journal of Polymer Science. Part A. Polymer Chemistry. 2010;**48**:4823-4834. DOI: 10.1002/pola.24273

[52] Gugel D, Niesner D, Eickhoff C, Wagner S, Weinelt M, Fauster T. Two-photon photoemission from image-potential states of epitaxial graphene. 2D Materials. 2015;**2**:045001. DOI: 10.1088/2053-1583/2/4/045001

[53] Schwierz F. Graphene transistors. Nature Nanotechnology. 2010;**5**:487-496. DOI: 10.1038/nnano.2010.89

[54] Ferrari AC. Raman spectroscopy of graphene and graphite: Disorder, electron–phonon coupling, doping and nonadiabatic effects. Solid State Communications. 2007;**143**:47-57. DOI: 10.1016/j.ssc.2007.03.052

[55] Wang QH, Jin Z, Kim KK, Hilmer AJ, Paulus GLC, Shih CJ, et al. Understanding and controlling the substrate effect on graphene electron-transfer chemistry via reactivity imprint lithography. Nature Chemistry. 2012;**4**:724-732. DOI: 10.1038/NCHEM.1421

[56] Cançado LG, Jorio A, Martins Ferreira EH, Stavale F, Achete CA, Capaz RB, et al. Quantifying defects in graphene via Raman spectroscopy at different excitation energies. Nano Letters. 2011;**11**:3190-3196. DOI: 10.1021/nl201432g

[57] Huang S, Dakhchoune M, Luo W, Oveisi E, He G, Rezaei M, et al. Single-layer graphene membranes by crack-free transfer for gas mixture separation. Nature Communications. 2018;**9**:2632-2642. DOI: 10.1038/s41467-018-04904-3

[58] Kim DW, Kim YH, Jeong HS, Jung HT. Direct visualization of large-area graphene domains and boundaries by optical birefringency. Nature Nanotechnology. 2012;**7**:29-34. DOI: 10.1038/nnano.2011.198

[59] Huang PY, Ruiz-Vargas CS, van der Zande AM, Whitney WS, Levendorf MP, Kevek JW, et al. Grains and grain boundaries in single-layer graphene atomic patchwork quilts. Nature. 2011;**469**:389-392. DOI: 10.1038/nature09718

[60] Nemes-Incze P, Yoo KJ, Tapasztó L, Dobrik G, Lábár J, Horváth ZE, et al. Revealing the grain structure of graphene grown by chemical vapor deposition. Applied Physics Letters. 2011;**99**:023104. DOI: 10.1063/1.3610941

[61] Li SH, Xu Z, Yang G, Ma L, Yang Y. Solution-processed poly(3-hexylthiophene) vertical organic transistor. Applied Physics Letters. 2008;**93**:213301. DOI: 10.1063/1.3030990

[62] Tsujioka T, Fujii H, Hamada Y, Takahashi H. Driving duty ratio dependence of lifetime of tris(8-hydroxy-quinolinate)aluminum-based organic light-emitting diodes. Japanese Journal of Applied Physics. 2001;**40**:2523-2526. DOI: 10.1143/jjap.40.2523

[63] Köhler A, Bässler H. Handbook of Electronic Processes in Organic Semiconductors: An Introduction. Weinheim, Germany: Wiley-VCH Verlag GmbH & Co. KGaA; 2015. pp. 424. DOI: 10.1002/9783527685172

[64] Fowler RH, Nordheim L. Electron emission in intense electric fields. Proceedings of the Royal Society A. 1928;**119**:173-181. DOI: 10.1098/rspa.1928.0091

[65] Sze SM. Handbook of Physics of Semiconductor Devices. 2nd ed. Hoboken, New Jersey: John Wiley & Sons, Inc.; 1981 868 pp

[66] Chiguvare Z, Parisi J, Dyakonov V. Current limiting mechanisms in indium-tin-oxide/poly3-hexylthiophene/aluminum thin film devices. Journal of Applied Physics. 2003;**94**:2440-2448. DOI: 10.1063/1.1588358

[67] Blum R, Sprave M, Sablotny J, Eich M. High-electric-field poling of nonlinear optical polymers. Journal of the Optical Society of America B. 1998;**15**:318-328. DOI: 10.1364/josab.15.000318

[68] Saker BK, Khondaker SI. Thermionic emission and tunneling at carbon nanotube-organic semiconductor interface. ACS Nano. 2012;**6**:4993-4999. DOI: 10.1021/nn300544v

[69] Yang H, Heo J, Park S, Song HJ, Seo DH, Byun KE, et al. Graphene Barristor, a triode device with a gate-controlled Schottky barrier. Science. 2012;**336**:1140-1143. DOI: 10.1126/science.1220527

[70] Bartolomeo AD. Graphene Schottky diodes: An experimental review of the rectifying graphene/semiconductor heterojunction. Physics Reports. 2016;**606**:1-68. DOI: 10.1016/j.physrep.2015.10.003

[71] Hsueh HY, Yao CT, Ho RM. Well-ordered nanohybrids and nanoporous materials from gyroid block copolymer templates. Chemical Society Reviews. 2015;**44**:1974-2018. DOI: 10.1039/C4CS00424H

[72] Chang SC, Liu J, Bharathan J, Yang Y, Onohara J, Kido J. Multicolor organic light-emitting diodes processed by hybrid inkjet printing. Advanced Materials. 1999;**11**:734-737. DOI: 10.1002/(SICI)1521-4095(199906)11:9<734::AID-ADMA734>3.0.CO;2-D

[73] Singh M, Haverinen HM, Dhagat P, Jabbour GE. Inkjet printing-process and its applications. Advanced Materials. 2010;**22**:673-685. DOI: 10.1002/adma.200901141

[74] Wang J, Song C, Zhong Z, Hu Z, Han S, Xu W, et al. In situ patterning of microgrooves via inkjet etching for a solution-processed OLED display. Journal of Materials Chemistry C. 2017;**5**:5005-5009. DOI: 10.1039/C7TC01330B